Numerical Analysis of Aluminum Alloy Reticulated Shells with Gusset Joints under Fire Conditions

Shaojun Zhu[1], Zhangjianing Cheng[1], Chaozhong Zhang[1], Xiaonong Guo[1*]

[1] College of Civil Engineering, Tongji University, Shanghai 200092, China

Abstract

This paper conducts numerical analysis on aluminum alloy reticulated shells (AARSs) with gusset joints under fire conditions. Firstly, the thermal-structural coupled analysis model of AARSs considering joint semi-rigidity is proposed and validated against the room-temperature and fire tests. The proposed model can also be adopted to analyze the fire response of other reticulated structures with semi-rigid joints. Secondly, parametric analysis is carried out based on the numerical model to explore the buckling behavior of K6 AARS with gusset joints under fire conditions. The results indicate that the span, height-to-span ratio, height of the supporting structure, and fire power are influential in the reduction factor of the buckling capacity of AARSs under fire conditions. In contrast, the reduction factor is independent of the number of element divisions, the number of rings, the span-to-thickness ratio, and the support condition. Subsequently, practical design formulae for predicting the reduction factor of buckling capacity of K6 AARSs are derived based on numerical analysis results and machine learning techniques to provide a rapid evaluation method. Finally, further numerical analyses are conducted to propose practical design suggestions, including the conditions of ignoring the ultimate bearing capacity analysis of K6 AARSs and ignoring the radiative heat flux.

Keywords

aluminum alloy reticulated shell, gusset joint, numerical analysis, fire resistance

1 Introduction

Aluminum alloys are increasingly applied in large-space spatial structures owing to their advantages of corrosion resistance, high strength-to-weight ratio, and favorable appearance. As one of the most popular structural types of aluminum alloy structures, single-layer reticulated shells can have multiple and even complex structural forms to adapt to aesthetic requirements, e.g., spherical shells, cylindrical shells, and free-form shells. Hence, traditional fire design concerning the resistance of structural components may not be economical [1]. In order to resolve this problem, the concept of performance-based fire resistance design is proposed, which calls for evaluation of the structural performance objectives, e.g., resistance or residual deformation of a specific structure or its structural components, under the designed fire scenarios.

Large-space fires differ from compartment fires since the volume of the fire is significantly smaller than that of the interior space, and the air temperature cannot be regarded as uniformly distributed. Hence, a large-space fire scenario firstly generates a non-uniformly distributed air temperature field. Then, the structural components receive the heat flux from the air and the fire through heat convection and radiation. Finally, the thermal expansion and changes in material properties cause the responses of the structure. Therefore, the performance-based fire resistance design for large-space fire scenarios requires data, including the air temperature field, the temperature development of structural components, and the structural response.

Conducting fire tests is the most direct way to obtain the data mentioned above. Despite the fire tests on different types of steel structures [2–8], fire tests on aluminum alloy structures have also been carried out in recent years. Guo *et al*. [9] conducted fire tests on a scale single-layer spherical aluminum alloy reticulated shell (AARS), where 8 large-space fire scenarios were designed. No damage to the shell specimen was observed after the fire tests, and the structural displacement was proved elastic. Then, Zhu *et al*. [10] proceeded with 2 destructive tests on the same shell specimen. The failure mode of the shell specimen under the designed fire scenario was the collapse, and the structural components failed by melting, rupture, and flexural-torsional buckling. As the aforementioned 2 studies focused on spherical reticulated shells, Yin *et al*. [11] designed a full-scale fire test on a cylindrical AARS specimen to evaluate the air temperature field. The test results revealed that the critical air temperature when the specimen collapsed was 330 ℃, indicating that the existing suggestion on the critical temperature limit, i.e., 150 ℃, has a large safety of margin.

Although fire tests can produce immediate data, they consume considerable time and resources. As the fire tests conducted in references [9–11] all recorded the thermal or structural responses of the specimen, it is possible to simulate the fire process using numerical analysis, including the air temperature field, the temperature development of the structural components, and the global structural response. Regarding the simulation of the air temperature field, references [9] and [11] used the field simulation software FDS and the existing empirical formula proposed by Du and Li [13]. The comparison indicated that the field simulation can produce a relatively accurate prediction of the air temperature field, yet the parameters in the empirical formula should be reasonably adjusted. As for the simulation of temperature development of aluminum alloy structural components, Zhu *et al*. [14] proposed an iterative calculation method and highlighted that the radiative heat flux produced by the fire in large-space fire scenarios cannot be ignored. Nonetheless, the simulation method of the structural response of aluminum alloy structures, i.e., the thermal-structural coupled analysis method, has not been proposed, which dramatically interferes with the performance-based fire resistance design process and the promotion of aluminum alloy structures. Notably, typical joint systems of aluminum alloy structures, such as the gusset joint system, are usually semi-rigid [15–18], and their semi-rigidity has been proved to be influential to the structural performance under room temperature [19]. However, the numerical model established for AARSs under room temperature [20, 21] cannot be directly applied to fire analysis since a temperature-dependent variation of the joint rigidity is included [22].

In addition, it is notable that in the performance-based fire resistance design, the field simulation and the thermal-structural coupled analysis are computationally expensive and are not friendly to practical engineers at the initial/concept design stage. Specifically, repeated thermal-structural coupled analyses are needed if the cross-sections of the members are adjusted, and additional field simulations are included if the fire scenario is adjusted due to changes in the architectural composition. The above problems call for rapid evaluation methods and practical design suggestions to provide valuable information for designers at the initial/concept design stage.

This paper conducts numerical analysis on AARSs with semi-rigid gusset joints under fire conditions. Firstly, the numerical model of AARSs under room temperature and its restrictions are briefly reviewed. Secondly, the numerical model for fire analysis is proposed and validated against the fire test data. Then, parametric analysis of the ultimate bearing capacity of K6 AARSs under fire conditions is conducted based on the validated thermal-structural coupled analysis model, and corresponding mechanisms are analyzed. Practical design formula for predicting the ultimate bearing capacity of K6 AARSs is proposed based on further numerical analysis and machine learning techniques. Finally, practical design suggestions, including the conditions of ignoring the ultimate bearing capacity analysis of K6 AARSs, and conditions of ignoring the radiative heat flux, are proposed based on further numerical analysis.

2 Numerical model

2.1 Model at room temperature and its restrictions

Based on a room-temperature static experiment on a K6 AARS specimen with semi-rigid gusset joints shown in Fig. 1 [23], Xiong *et al*. [20] established and verified the numerical model to simulate the stability behavior of the specimen using the general finite element software ANSYS [25]. In the numerical model, the BEAM188 element is used to simulate the member and the joint zone. It is noteworthy that due to the existence of the joint plate, the out-of-plane bending stiffness of the joint zone is significantly larger than that of the member. Thus, the elastic modulus of the element at the joint zone is set as 100E, where E is the elastic modulus of the member. Note that the value of 100 is determined based on trial and error [20]. The two-node non-linear spring element COMBIN39 is used to simulate the out-of-plane bending stiffness of the gusset joint, where the non-linear stiffness parameters are calculated by the four-line model proposed by Guo *et al*. [26]. In order to save the computational cost, the other degrees-of-freedoms (DOFs), including the 3 translational DOFs, the in-plane, torsional rotational DOFs, and the warping DOF, are coupled between the member and the joint zone.

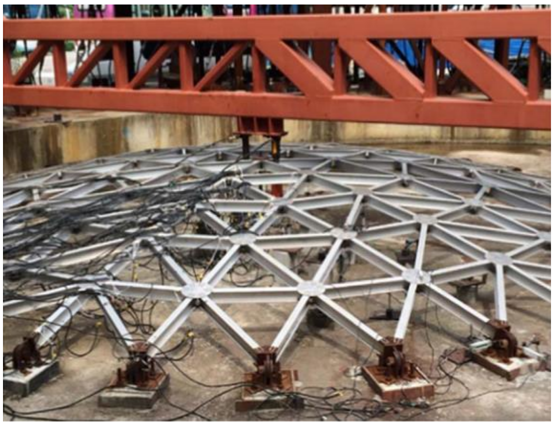

Fig. 1 Room-temperature static test specimen of a K6 AARS [23].

Through experimental and numerical investigation, Guo *et al*. [22] highlighted that the rigidity of the gusset joint is dependent on the temperature. However, the real constants of the COMBIN39 element, i.e., the out-of-plane bending stiffness of the joint, cannot be varied through the analysis directly or indirectly, e.g., via the birth and death element method. Therefore, the numerical model under room temperature cannot be directly applied to fire analysis.

2.2 Numerical model for fire analysis

In order to consider the temperature-dependent joint rigidity, the MPC184 element, which is a multi-point constraint element based on the Lagrange multiplier method, is used to replace the COMBIN39 element in the room-temperature numerical model. In specific, the pin sub-element shown in Fig. 2 is adopted. The pin sub-element is a two-node single-degree-of-freedom element, which can rotate around axis 1 of the local coordinate system of nodes *i* and *j*. In Fig. 2, $\mathbf{e}_{m,i}$ and $\mathbf{e}_{m,j}$ are the unit vectors of nodes *i* and *j* in the *m* direction (*m* = 1, 2, 3) of their local coordinate systems, respectively. Denote $\mathbf{u}_i$ and $\mathbf{u}_j$ as the resultant displacement vectors of nodes *i* and *j*, respectively, and the constraint conditions of the pin element can be described as

$$\begin{cases} \mathbf{u}_i = \mathbf{u}_j \\ \mathbf{e}_{1,i} \cdot \mathbf{e}_{2,j} = 0 \\ \mathbf{e}_{1,i} \cdot \mathbf{e}_{3,j} = 0 \end{cases} \tag{1}$$

The non-linear stiffness, damping properties, and Coulomb friction of the pin element at different temperatures can be simulated by defining the material properties. The element also supports geometric non-linear analysis and linear perturbation analysis.

When using the pin sub-element of the MPC184 element to simulate the non-linear bending stiffness of the gusset joint, the following points should be noted:

(1) The two nodes of the element must have the same spatial coordinates;
(2) After defining an element, the SECDATA command must be used to define a shared local coordinate system for both nodes;
(3) Use the JOIN option in the TB command to define the non-linear moment-rotation curve of the joint, and input the points on the curve by the TBDATA command;
(4) Use the TBTEMP command to shift different temperatures for the moment-rotation curves.

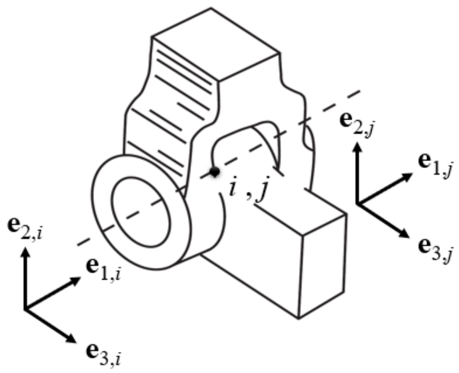

Fig. 2 Pin sub-element of the MPC184 element [25].

Therefore, the simplified numerical model for a member in AARSs is established as shown in Fig. 3, where the elements selected for the member and the joint zone are the same as described in Section 2.1. Note that we do not consider the stiffness reduction of the joint zone due to the elevated temperature, as no joints fail before the members in the fire test conducted in literature [10].

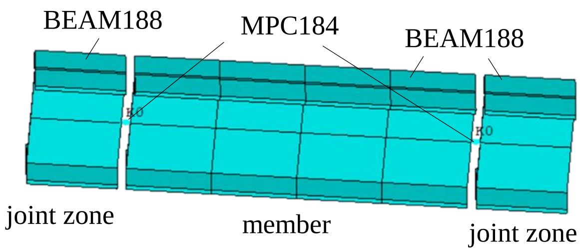

Fig. 3 Simplified numerical model for a member in the AARS.

2.3 Validation of the model for fire analysis

As the proposed numerical model for fire analysis is adaptive to the bending stiffness of the joint under different temperatures, this section verifies the model using the room-temperature test data [23] and the fire test data [10].

a) Room-temperature test

Fig. 4 shows the comparison of the load-displacement curve of the top joint of the shell specimen obtained by the experimental data and the proposed numerical model, where P is the load and δ is the vertical displacement. As the curve obtained by the proposed model is in good agreement with the experimental curve, it can be concluded that the proposed numerical model is also reliable in simulating the buckling behavior of reticulated shells with semi-rigid joints at room temperature.

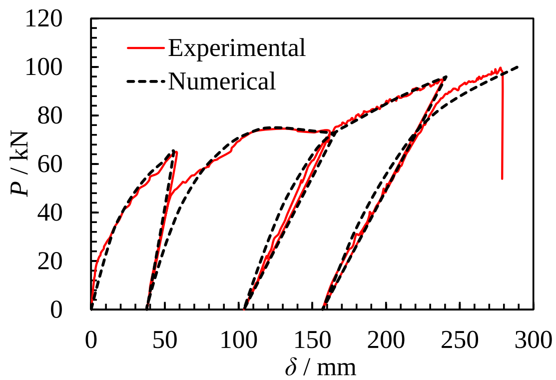

Fig. 4 Comparison of load-displacement curves obtained by test and numerical simulation.

b) Fire test

Fig. 5 (a) plots the material constitutive model of the 6063-T5 aluminum alloy used for the AARS specimen in reference [10]. Notably, the elastic modulus and nominal yield strength of the material at 600°C are set as 1% of those under room temperature to simulate the melting of the material. Based on the out-of-plane bending stiffness model of aluminum alloy gusset joints at elevated temperatures [22], the out-of-plane moment-rotation curves of the joints in the AARS specimen [10] at different temperatures are calculated as shown in Fig. 5(b). Note that the elevated-temperature constitutive model shown in Fig. 5(b) is determined by the room-temperature tensile test conducted in literature [10], the elevated-temperature material property reduction factors, and constitutive models recommended in the Eurocode 9 [24].

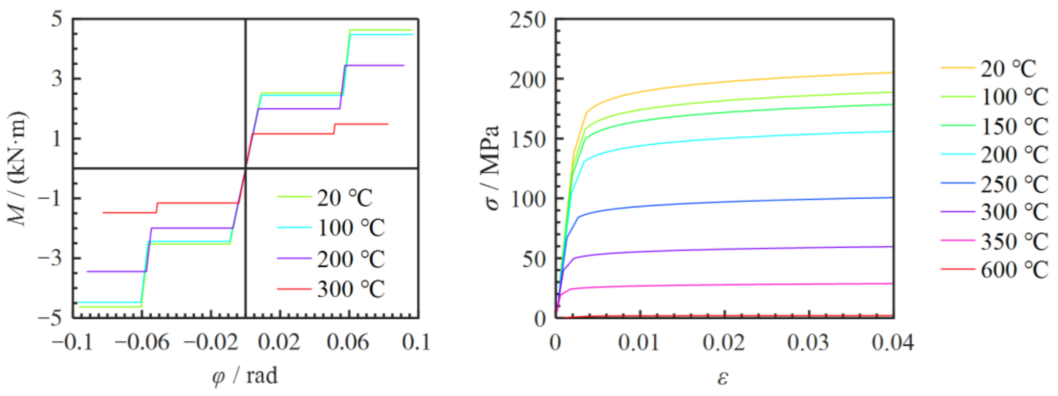

(a) Material constitutive model (b) Out-of-plane bending stiffness of the joint

Fig. 5 Properties of material and joint in the AARS shell specimen tested in literature [10] at different temperatures

Destructive fire tests D-1 and D-2 in reference [10] are used for validating the established numerical model since the deformation of the specimen is large. The stable combustion state of the two tests is exhibited in Fig. 6. By introducing the measured member temperature data to the numerical model, the comparison of the experimental and numerical displacement-time curves of typical joints in the AARS specimen in fire tests D-1 and D-2 [10] are shown in Figs. 7 and 8, respectively, where the upward displacement is positive. Note that D*i* is the symbol of the *i*th displacement transducer, whose detailed location is given in reference [10]. Besides, only the displacement curves before the fire became very faint in test D-1 are introduced in Fig. 7, i.e., the time range is 0 s ~ 800 s. The comparison of the numerical and experimental deformation of the specimen is shown in Fig. 9. It can be concluded from the good agreement of the curves and the identical deformation patterns that the proposed numerical model is able to simulate the thermal expansion, stiffness degradation, and the fire-induced collapse of AARS with semi-rigid gusset joints. Notably, the numerical simulation of test D-2 is terminated at the end of the test, i.e., at 614 s, while the photo shows the ultimate deformation when the fire is finally extinct. Although there are slight differences, it can still be concluded that the sinking deformation at the center of the specimen within the fire duration has been well simulated.

The proposed model can also be used to simulate the buckling behavior of other types of reticulated structures with semi-rigid joints under fire conditions when different bending stiffness models are introduced for the MPC184 element.

(a) Test D-1 (b) Test D-2

Fig. 6 Stable combustion state of the two fire tests used for validation [10]

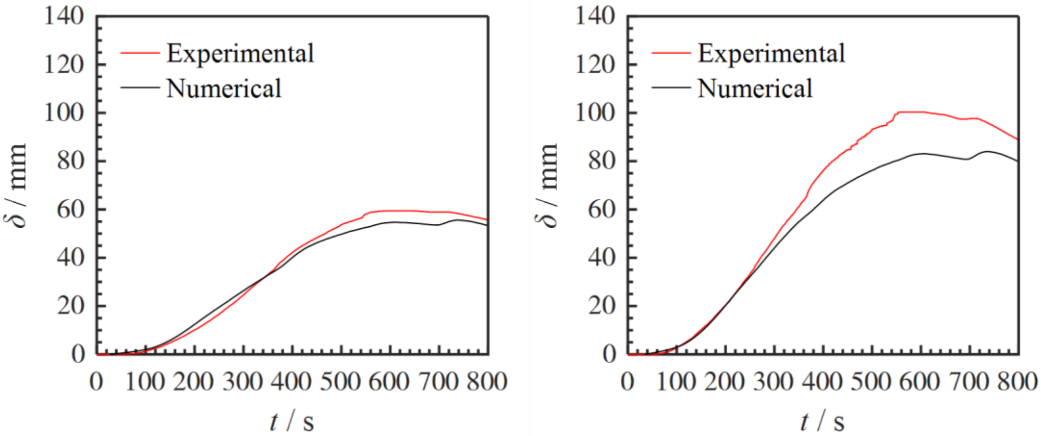

(a) D1 (b) D2

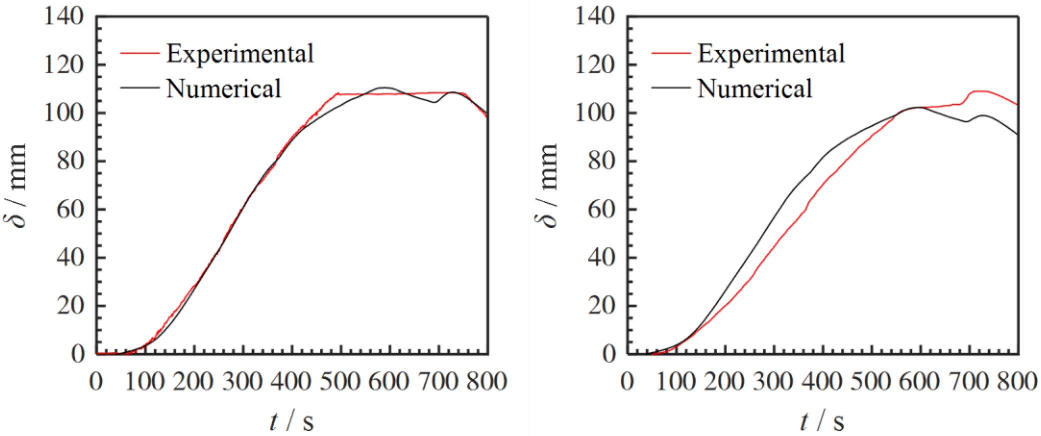

(c) D6 (d) D7

Fig. 7 Comparison of experimental and numerical displacement-time curves of typical joints in test D-1

As the readings of the displacement sensors have been reset to zero before tests D-1 and D-2, the displacement induced by the vertical load applied before the tests will not influence the comparison shown in Figs. 7 and 8.

3 Parametric study

Zhu *et al*. [10] analyzed the mechanism of the fire-induced collapse of K6 AARSs. They concluded that the *ferrule effect* is the main cause of the thermal compressive forces of the ring members. The failure of the structure is the outcome of degradation of material properties, the ferrule effect, and the catenary action.

As the K6 reticulated shell is one of the most commonly-used spatial structural types, this section further investigates the ultimate bearing capacity of K6 AARS with gusset joints under fire conditions, based on the proposed numerical model. The main motivation is that the ultimate bearing capacity of the structure is also concerned in the performance-based fire resistance design. In order to illustrate the variation in the ultimate bearing capacity during the fire process, we define $k_\Lambda(t)$ as the reduction factor of the ultimate bearing capacity at time t of the fire process, calculated by

$$k_\Lambda(t) = \frac{\Lambda(t)}{\Lambda(0)} \tag{2}$$

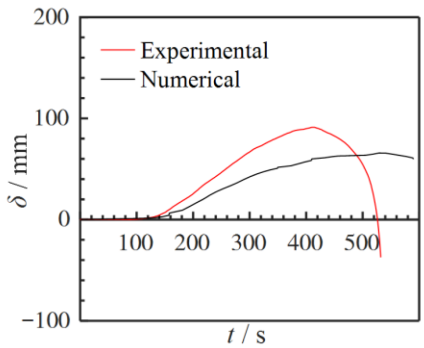

(a) D1

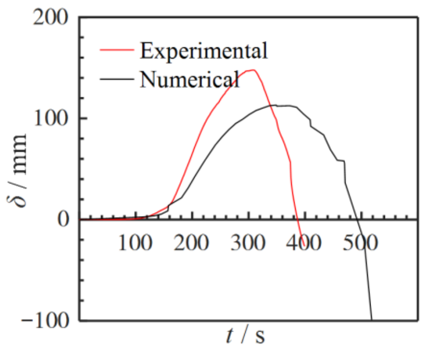

(b) D5

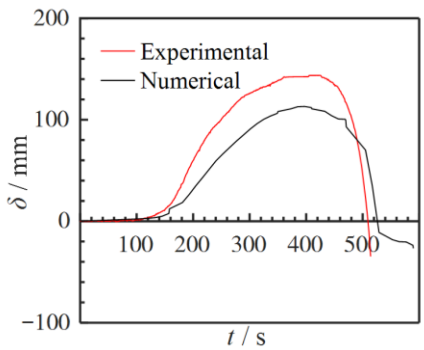

(c) D6

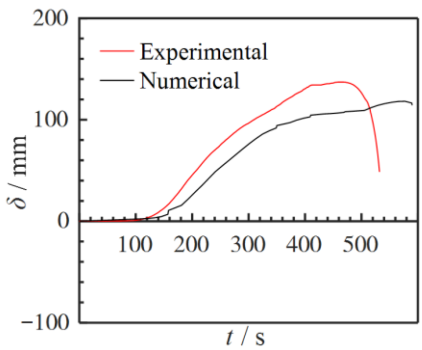

(d) D7

Fig. 8 Comparison of experimental and numerical displacement-time curves of typical joints in test D-2

where $\Lambda(0)$ and $\Lambda(t)$ are the elasto-plastic buckling capacity of AARS with gusset joints at times 0 and t of the fire process, respectively. Note that $\Lambda(0)$, i.e., the room-temperature buckling capacity, can be calculated based on the formulae proposed in reference [20] or the room-temperature numerical model introduced in Section 2.1, while $\Lambda(t)$ should be determined based on the numerical model proposed in Section 2.2.

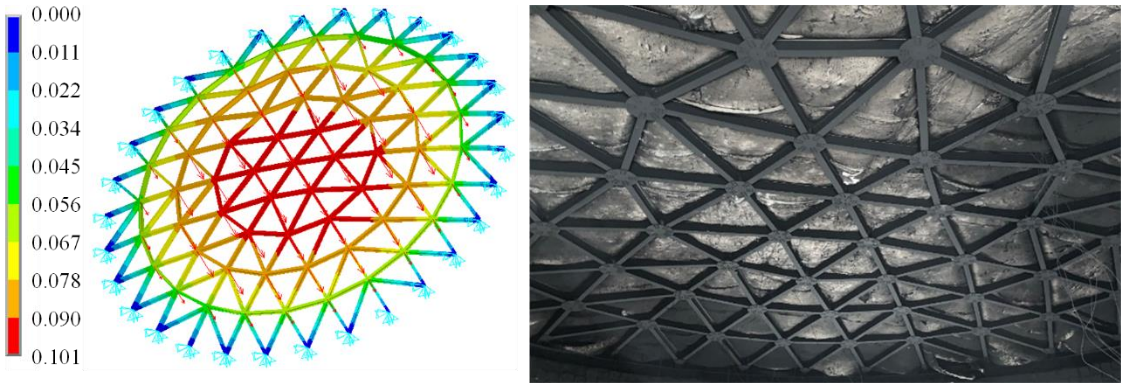

(a) Test D-1

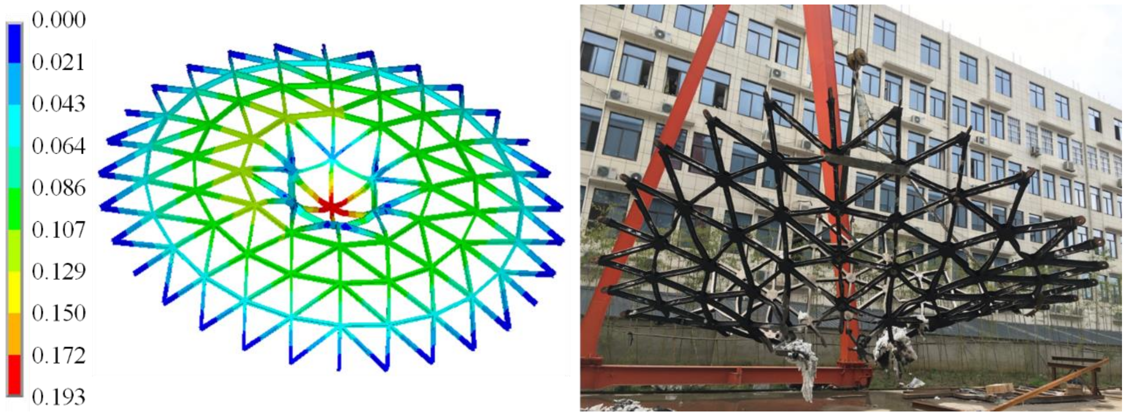

(b) Test D-2

Fig. 9 Comparison of experimental and numerical deformation patterns

3.1 Analysis scheme

In order to explore the calculation method of $k_\Lambda(t)$ (abbreviated as k_Λ hereinafter) under common fire conditions, numerical models are established based on the following analysis scheme:

(1) Span L: 25, 30, 40 m;
(2) Height-to-span ratio f/L: 1/3, 1/4, 1/5;
(3) Number of rings: 10, 12, 14;
(4) Cross-section: H250×200×8×10, H300×200×10×14, and H400×250×10×16;
(5) Support conditions: pinned support, fixed support at the periphery;
(6) Fire power Q: 2, 8, 25 MW;
(7) Height of the supporting structure H: 0, 5, 10 m;
(8) Fire location: at the center (location 1), at the corner (location 2).

Note that items (1), (2), (3), and (5) are determined according to the engineering experience, while the cross-section of the members, i.e., item (4), is determined based on the principle of avoiding the in-plane buckling of the member [27] and local buckling of the cross-section [28]. Identical cross-sections are assigned for all the members because the gusset joint requires the height of the H-shaped members to be exactly the same. Illustrations of some parameters are shown in Fig. 10.

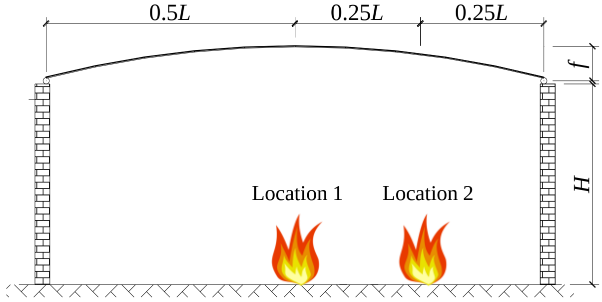

Fig. 10 Numerical model parameters

According to the heat release rate-time curves of ordinary large-space fire combustibles given in the NFPA handbook [29], the fire duration will not exceed 2000 s. In order to study the variation trend of the elasto-plastic ultimate bearing capacity of AARSs under the whole fire process, the fire duration t_{max} is selected as 2400 s, and the interval of the evaluation of the ultimate bearing capacity is 240 s, considering both the accuracy and the computational cost.

The empirical formula proposed by Du and Li [13] without the drop in the temperature is used to calculate the air temperature field as suggested by reference [9]. The temperature development of aluminum alloy structural components is calculated according to the point assumption-based method proposed in reference [14].

The 6061-T6 aluminum alloy is selected as the material of the numerical model. Its material properties at room and elevated temperatures are determined according to the Eurocode [24].

3.2 Influence of number of element divisions

Member buckling directly influences the global stability of reticulated shells [30], which can be simulated by simulating a member with multiple elements [31]. However, increasing the number of element divisions greatly affects the total number of nodes and elements in the numerical model, resulting in a higher computational cost. Therefore, this section investigates the influence of the number of element divisions on the reduction factor k_Λ.

Fig. 11 shows the k_Λ-t curves of the two fire locations when different numbers of segments are used to simulate the member, respectively. The span of the numerical model is 40 m, the height-to-span ratio is 1/3, the cross-section is H400×250×10×16, the number of rings is 12, the support condition is pinned support, the height of the supporting structure is 0 m, and the fire power is 8 MW. It can be seen that the k_Λ-t curves are coincident when the number of element divisions increases from 1 to 4, indicating that k_Λ is independent of the number of element divisions. Note that the parameters not specifically described in the following sections are the same as those mentioned above.

This is because the cross-sections are designed to prevent member buckling and local buckling, as discussed in Section 3.1. Therefore, there will be no interaction between member buckling and global buckling in the numerical examples. To reduce the computational cost, only one element will be used to simulate the member in the following numerical analysis. Meanwhile, the shape function of the element adopts cubic polynomial to ensure accuracy.

3.3 Influence of span

When the height-to-span ratio and the span-to-thickness ratio, i.e., the ratio of the span to the height of the member, are constant, the span influences the distribution of the air temperature field. Fig. 12 shows the k_Λ-t curves of the two fire locations with different spans, i.e., 25, 30, and 40 m.

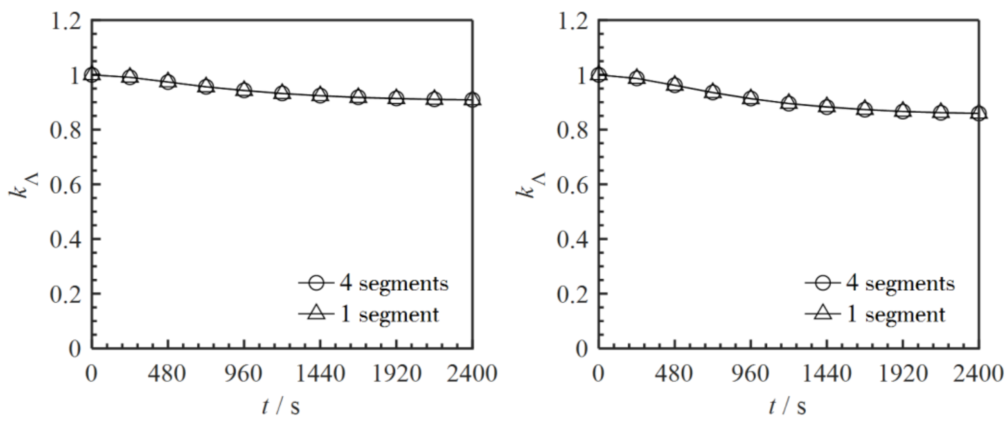

(a) Fire location 1 (b) Fire location 2

Fig. 11 Influence of number of element divisions on k_Λ

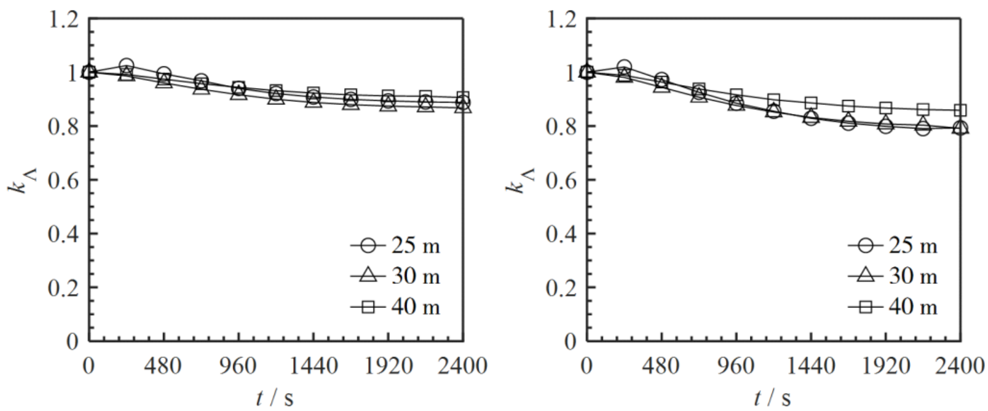

(a) Fire location 1 (b) Fire location 2

Fig. 12 Influence of span on k_Λ

The following conclusions can be obtained from Fig. 12:

(1) When the span is 25 m, k_Λ increases at the initial stage of the fire process, while the value of k_Λ monotonically decreases with the time when the span is 30 m or 40 m. This is because the air temperature field and the thermal expansion are more uniformly distributed when the span is smaller. As the maximum temperature of structural components is relatively small at the initial stage of the fire process, the reduction in the material properties is not significant. At this time, the thermal expansion can be regarded as a minor variation in the structural shape, which can result in an increase in the ultimate bearing capacity [32];

(2) When the fire location moves from the center to the corner, k_Λ greatly decreases at the late stage of the fire process, while the reduction in k_Λ becomes less significant with the increase of the span. This is because the asymmetric air temperature field induced by the fire at the corner is more disadvantageous than the symmetric air temperature field induced by the fire at the center, and the extra compressive forces due to the ferrule effect become more severe.

3.4 Influence of height-to-span ratio

The shape of spherical AARSs is determined by the height-to-span ratio, which also affects the global stability [20] and the air temperature field. Fig. 13 shows the k_Λ-t curves of the two fire locations under various height-to-span ratios, i.e., 1/3, 1/4, and 1/5.

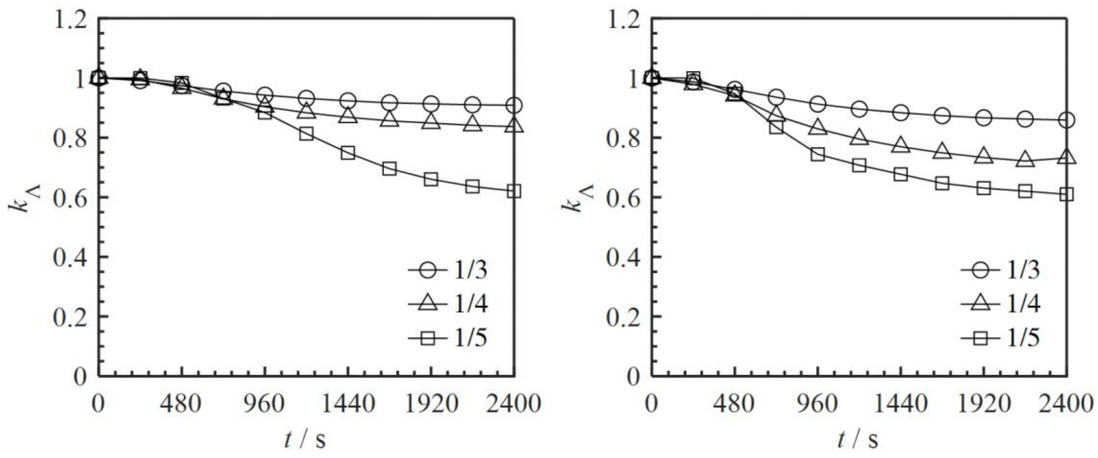

(a) Fire location 1 (b) Fire location 2

Fig. 13 Influence of height-to-span ratios on k_{Λ}

The following conclusions can be obtained from Fig. 13:

(1) With the decrease of the height-to-span ratio, k_{Λ} gradually decreases simultaneously within the fire process. Therefore, the reduction in the ultimate bearing capacity of AARSs with small height-to-span ratios is more severe under fire conditions. This is because the compressive forces induced by the ferrule effect are more unfavorable to AARSs with small height-to-span ratios. In specific, AARSs with small height-to-span ratios bear more external load through their bending stiffness instead of the membrane stiffness, so that they are more sensitive to the extra compressive forces, which result in a reduction in the bending stiffness [27]; in addition, as the top joint is closer to the fire source, the average temperature of structural components is higher, and the degradation in material properties is more dramatic;

(2) When the fire source moves from the center to the corner, k_{Λ} of AARSs with various height-to-span ratios all decrease, and the maximum decline occurs when the height-to-span ratio is 1/4. This is because when the fire source is located at the center, the favorable effect of the symmetric thermal expansion [9] can neutralize the reduction in the ultimate bearing capacity.

3.5 Influence of number of rings

The ultimate bearing capacity of K6 AARSs improves with the increase of the number of rings at room temperature [20]. Fig. 14 shows the k_{Λ}-t curves of the two fire locations under various numbers of rings, i.e., 10, 12, and 14. Note that the cross-section considered in this section is H300×200×10×14. It can be seen from Fig. 14 that the effect of the number of rings on k_{Λ} is not significant.

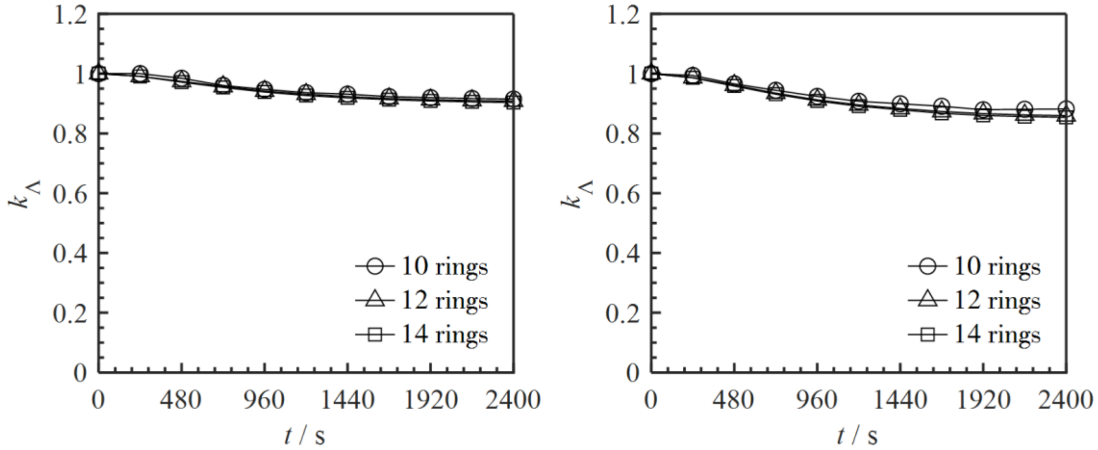

(a) Fire location 1 (b) Fire location 2

Fig. 14 Influence of number of rings on k_Λ

In order to explore the mechanism, Fig. 15 shows the ultimate states of the AARSs with different numbers of rings at t = 2400 s when the fire is located at the center. It can be observed that the shells share the same failure mechanism, which is excessive bulge deformation at the outmost ring. Notably, this failure mechanism is in accordance with the analysis by Zhu *et al*. [10], that the compressive forces of members at the outmost ring are the highest among all members due to the ferrule effect. In specific, although the ultimate bearing capacity of AARSs at room temperature can be increased by increasing the number of rings [20], the relative stiffness of the outmost ring almost remains unvaried, resulting in identical values of k_Λ. As a result, the number of rings will be taken as a constant value when deriving the formula of k_Λ in Section 4.

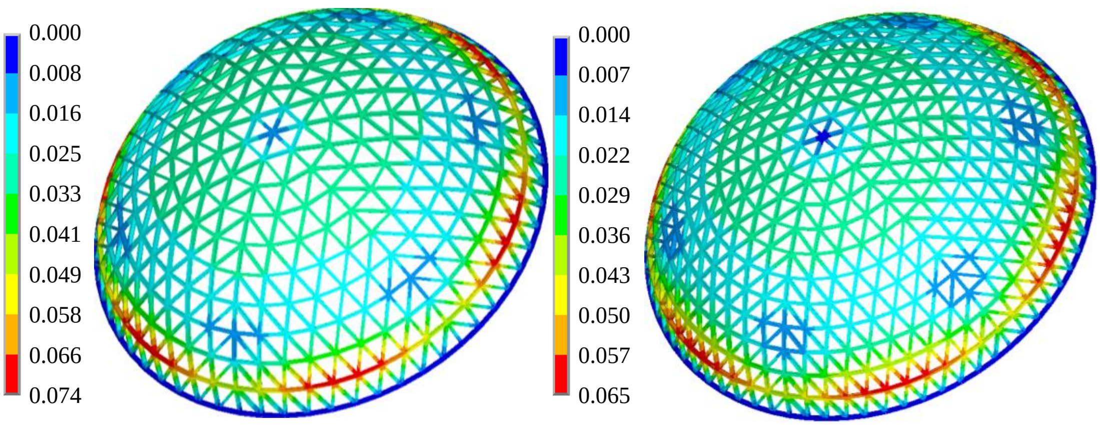

(a) 10 rings (b) 12 rings

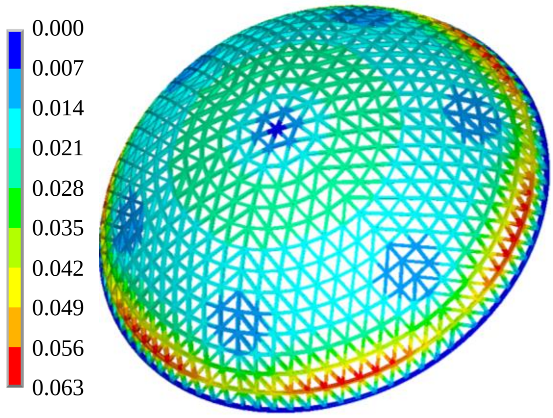

(c) 14 rings

Fig. 15 Ultimate states of AARSs with different numbers of rings at t = 2400 s (fire located at the center, unit: m)

3.6 Influence of span-to-thickness ratio

When the span is constant, the ultimate bearing capacity of a K6 AARS at room temperature increases with the decrease of the span-to-thickness ratio [20]. Fig. 16 shows the k_Λ-t curves of the two fire locations under different span-to-thickness ratios, i.e., 160, 300/4, and 100. As the span of the numerical model is 40 m, the corresponding cross-sections of the members are H250×200×8×10, H300×200×10×14, and H400×250×10×16, respectively.

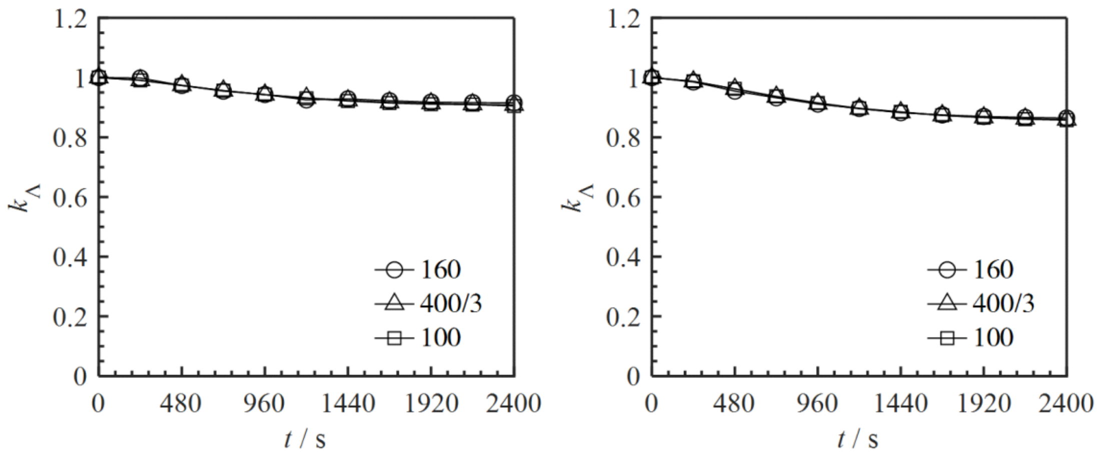

(a) Fire location 1 (b) Fire location 2

Fig. 16 Influence of span-to-thickness ratios on k_Λ

It can be seen from Fig. 16 that the k_Λ-t curves are almost coincident. Fig. 17 shows the ultimate states of the AARSs with different span-to-thickness ratios at t = 2400 s when the fire is located at the center. Notably, the ultimate state of the AARS with the span-to-thickness ratio of 400/3 is the same as in Fig. 15(b). The mechanism is almost the same as described in Section 3.5. Since member buckling has already been avoided, although enlarging the cross-section of the member leads to an increase in the global stiffness, the relative stiffness of the outmost ring is not changed. Therefore, the values of k_Λ remain unvaried. In this way, the span-to-thickness ratio will be taken as a constant value when deriving the formula of k_Λ in Section 4.

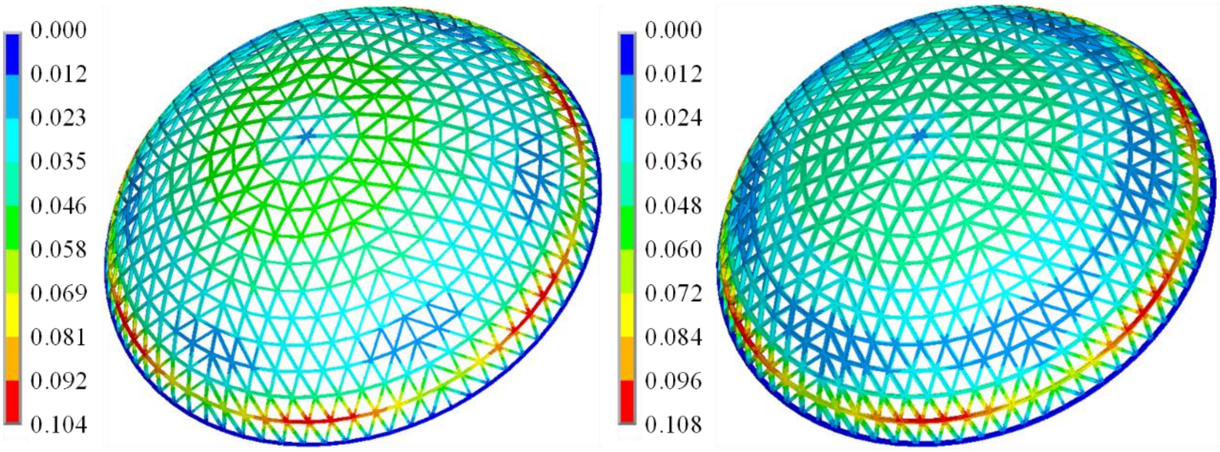

(a) 160 (b) 100

Fig. 17 Ultimate states of AARSs with different span-to-thickness ratios at t = 2400 s (fire located at the center, unit: m)

3.7 Influence of support condition

The support condition is influential to the room-temperature elasto-plastic buckling capacity of AARSs as there is an approximate 10% reduction in the buckling capacity when the support condition varies from fixed support to pinned support [20]. Fig. 18 shows the k_Λ-t curves of the two fire locations under different support conditions, i.e., pinned and fixed support. Note that the cross-section considered in this section is H250×200×8×10. It can be observed from Fig. 18 that the influence of support conditions on k_Λ is not significant.

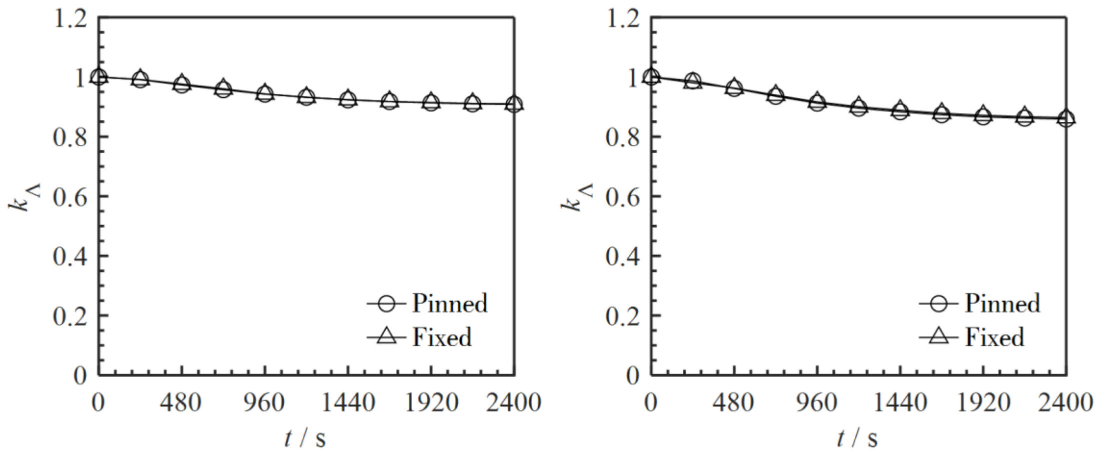

(a) Fire location 1 (b) Fire location 2

Fig. 18 Influence of support conditions on k_Λ

Fig. 19 shows the ultimate states of the AARSs with different support conditions at t = 2400 s when the fire is located at the center. It can be observed that the failure mode remains the same when the support conditions are different, i.e., the relative stiffness of the outmost ring is not changed by the support condition. Therefore, in the subsequent numerical analysis, only the pinned-supported AARSs will be analyzed in order to reduce the computational cost.

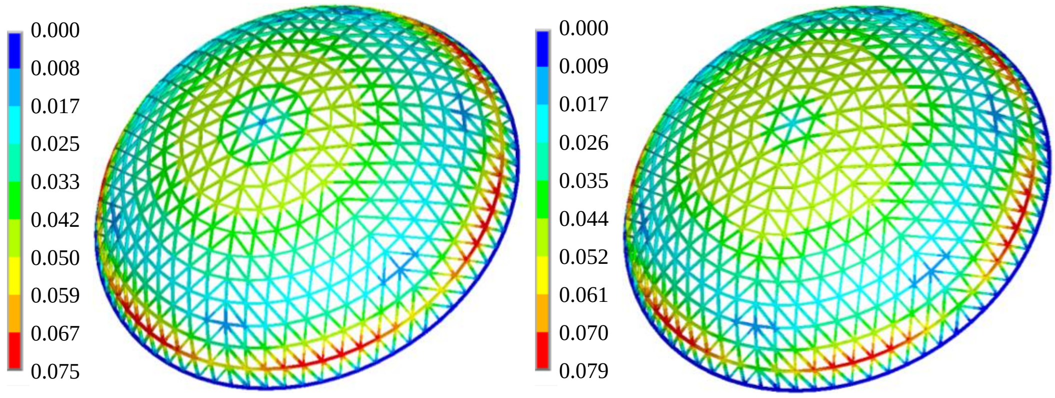

(a) Pinned support (b) Fixed support

Fig. 19 Ultimate states of AARSs with different support conditions at t = 2400 s (fire located at the center, unit: m)

3.8 Influence of height of supporting structure

The height of the supporting structure directly impacts the air temperature field. Fig. 20 shows the k_Λ-t curves of the two fire locations under different heights of the supporting structure, i.e., 0 m, 5 m, and 10 m. Note that the cross-section considered in this section is H300×200×10×14.

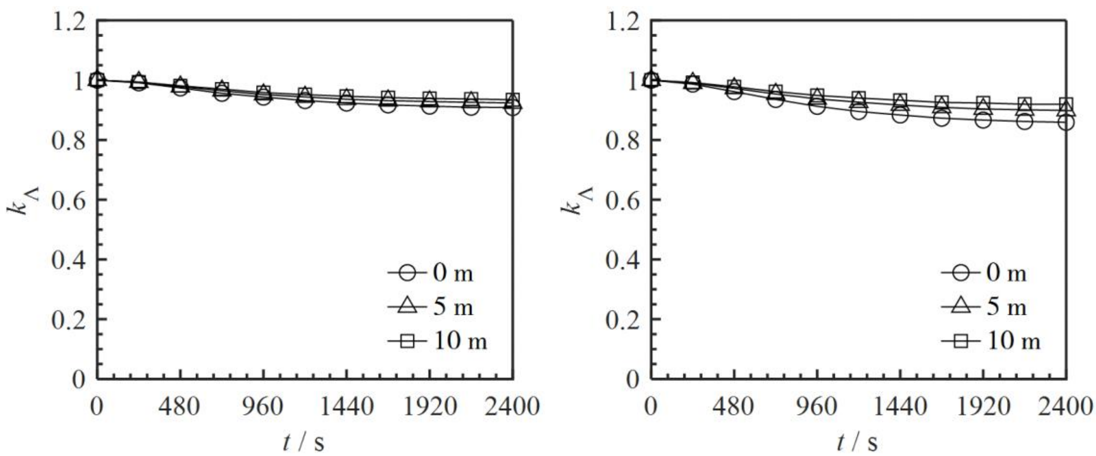

(a) Fire location 1 (b) Fire location 2

Fig. 20 Influence of height of supporting structure on k_Λ

The following conclusions can be obtained from Fig. 20:

(1) With the increase of the height of the supporting structure, k_Λ increases at each

time within the fire process. This is because the height of the supporting structure can also be regarded as the minimum distance between the fire source and the structural components. Hence, the air temperature near the structural components and the radiative heat flux from the fire source decrease [14]. As a result, the degradation in material properties, as well as the thermal compressive force induced by the ferrule effect, becomes less severe;

(2) With the increase in the height of the supporting structure, the increase rate of k_Λ is reduced. Therefore, the economic benefit of considerably adjusting the structural layout for ensuring fire safety is low for large-space structures.

3.9 Influence of fire power

The fire power directly affects the maximum temperature of the air temperature field [9]. Fig. 21 shows the k_Λ-t curves of the two fire locations under different fire powers, i.e., 2 MW, 8 MW, and 25 MW. Note that the cross-section considered in this section is H300×200×10×14.

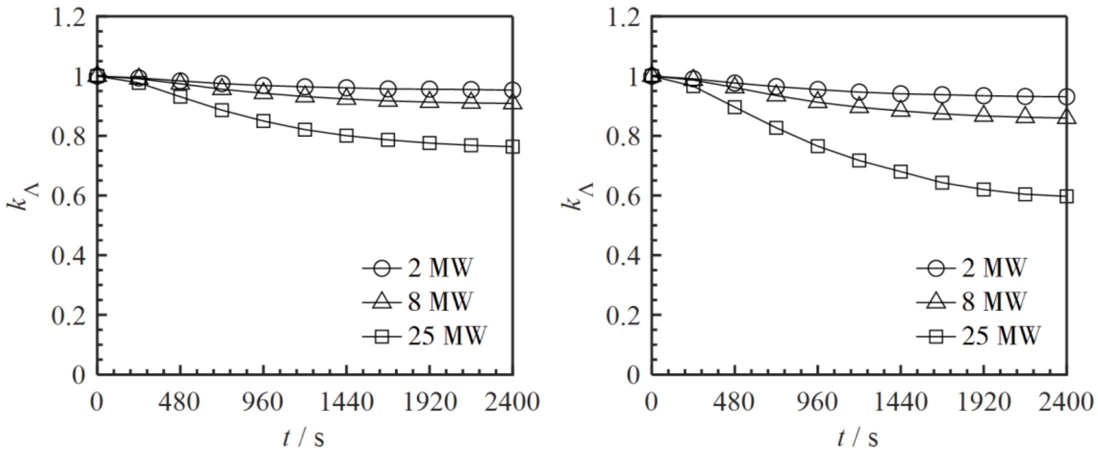

(a) Fire location 1 (b) Fire location 2

Fig. 21 Influence of fire power on k_Λ

It can be concluded from Fig. 21 that with the increase of the fire power, k_Λ decreases at each time of the fire process. This is due to the increase in the temperature at each height of the fire centerline and the radiative heat flux with the increase of the fire power. Therefore, the reduction in material properties and extra compressive forces caused by the high temperature becomes more significant, resulting in a more severe reduction in the ultimate bearing capacity.

4 Practical design formula

In the initial/concept design stage, it is necessary to predict the ultimate bearing capacity of AARSs under fire conditions. In this section, a practical design formula of the reduction coefficient k_Λ will be derived based on further parametric analysis.

4.1 Form of formula

The following rules can be obtained by observing the k_Λ-t curves in Sections 3.2 to 3.9:

(1) The value of k_Λ is 1.0 at 0 s as the fire has not affected the structure, i.e., $k_\Lambda(0) = 1.0$;

(2) The value of k_Λ almost decreases monotonously with time and reaches the minimum value $k_{\Lambda,\min}$ at the end of the fire process, i.e., $k_\Lambda(2400) = k_{\Lambda,\min}$;

(3) The value of k_Λ varies slowly at the early stage of the fire process, rapidly in the middle stage, and slowly again at the later stage. Hence, the k_Λ-t curve should include two inflection points.

Thus, the calculation formula of $k_\Lambda(t)$ can be constructed as

$$k_\Lambda\left(t\right) = \frac{k_{\Lambda,\min}}{1+\left(k_{\Lambda,\min}-1\right)\mathrm{e}^{-10^{-6}t^2}} \tag{3}$$

where t is the time (s) ranging in $0 \le t \le 2400$. It can be seen from Eq. (3) that the formula of $k_\Lambda(t)$ only contains one undetermined parameter $k_{\Lambda,\min}$. Take the curves of the fire power series in Section 3.9 as the example, and Fig. 22 shows the comparison between the numerical curve and the curve calculated by Eq. (3), when $k_{\Lambda,\min}$ is directly taken as the accurate result of the numerical curve. In Fig. 22, the solid red line represents the curve of Eq. (3). It can be seen that the form of Eq. (3) can accurately predict the variation of the reduction factor of the ultimate bearing capacity in the whole process of the fire. Thus, the equation of $k_\Lambda(t)$ can be determined based on two thermal-structural coupled elasto-plastic analyses, i.e., the calculation of $k_{\Lambda,\min}$.

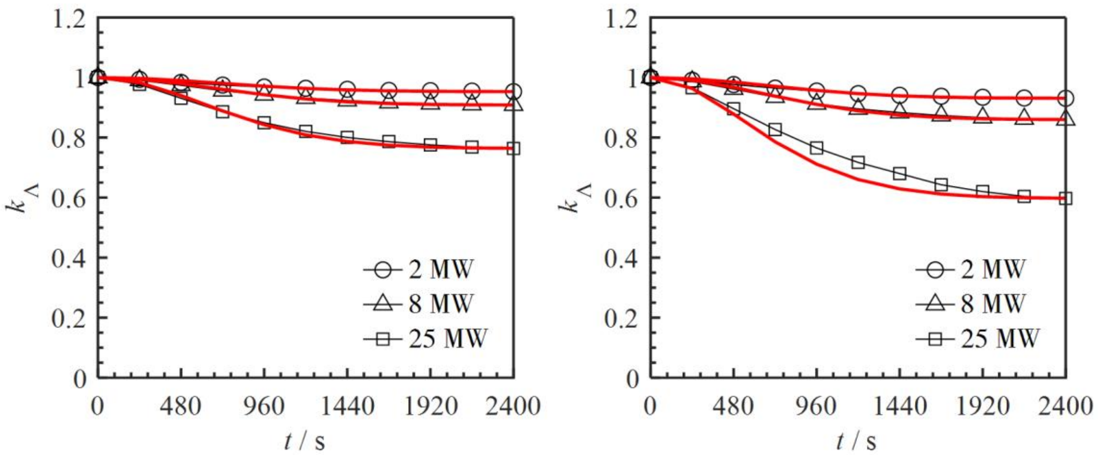

(a) Fire location 1 (b) Fire location 2

Fig. 22 Comparison of numerical curves and the curve of the proposed formula

4.2 Parametric analysis scheme

In order to further reduce the computational cost in practical engineering applications, the practical calculation method of $k_{\Lambda,\min}$ under common fire scenarios is expected to be proposed.

According to the parametric analysis in Sections 3.2 to 3.9, the value of k_Λ should be only related to the span, the height-to-span ratio, the height of the supporting structure, the fire power, and the fire location. As other parameters are kept constant, i.e., the number of rings is 12, the span-to-thickness ratio is 100, and the support condition is pinned support, the numerical models of 162 reticulated shells are established considering the following parameters:

(1) Span L: 25, 30, 40 m;
(2) Height-to-span ratio f/L: 1/3, 1/4, 1/5;
(3) Fire power Q: 2, 8, 25 MW;
(4) Height of supporting structure H: 0, 5, 10 m;
(5) Fire location: at the center (location 1), at the corner (location 2).

4.3 Regression based on machine learning

As indicated in Section 4.1, Λ(0) and Λ(2400) will be calculated in order to determine the value of $k_{\Lambda,\min}$ for each numerical model:

$$k_{\Lambda,\min} = \frac{\Lambda(2400)}{\Lambda(0)} \tag{4}$$

On this basis, using the Statistics and Machine Learning Toolbox in MATLAB R2020a [33], the support vector machine with a linear kernel function is used to fit the numerical results, while quadratic terms are introduced to improve the accuracy (see literature [31] for specific principles). Hence, $k_{\Lambda,\min}$ can be calculated as follows:

$$\begin{aligned} k_{\Lambda,\min} &= p_1 L + p_2\left(f/L\right) + p_3 Q + p_4 H + p_{1,1}L^2 + p_{1,2}L\cdot\left(f/L\right) + p_{1,3}L\cdot Q + p_{1,4}L\cdot H \\ &+ p_{2,2}\left(f/L\right)^2 + p_{2,3}\left(f/L\right)\cdot Q + p_{2,4}\left(f/L\right)\cdot H + p_{3,3}Q^2 + p_{3,4}Q\cdot H + p_{4,4}H^2 + b \end{aligned} \tag{5}$$

where p_i is the coefficient of the ith ($1 \le i \le 4$) linear term, $p_{i,j}$ is the coefficient of the ijth ($i \le j \le 4$) quadratic term, and b is the undetermined bias. For the two fire locations, the fitting values of each parameter in Eq. (5) are shown in Table 1. Denote the result calculated by Eq. (5) as the fitting value and the results calculated by the thermal-structural coupled analysis as the actual value. Fig. 23 shows the comparison of the fitting value and the actual value. It can be seen that the error is relatively small, and it is reasonable to use Eqs. (3) and (5), together with Table 1, to rapidly predict the ultimate bearing capacity at the initial stage of the design of AARSs. This way, repetitive thermal-structural coupled analyses under fire conditions can be avoided at the initial/concept design stage. However, it is worth noting that Eqs. (3) and (5) are only applicable to K6 AARSs when the span is 25 ~ 40 m, the height-to-span ratio is 1/5 ~ 1/3, the height of the supporting structure is 0 ~ 10 m, and the fire power is 2 ~ 8 MW.

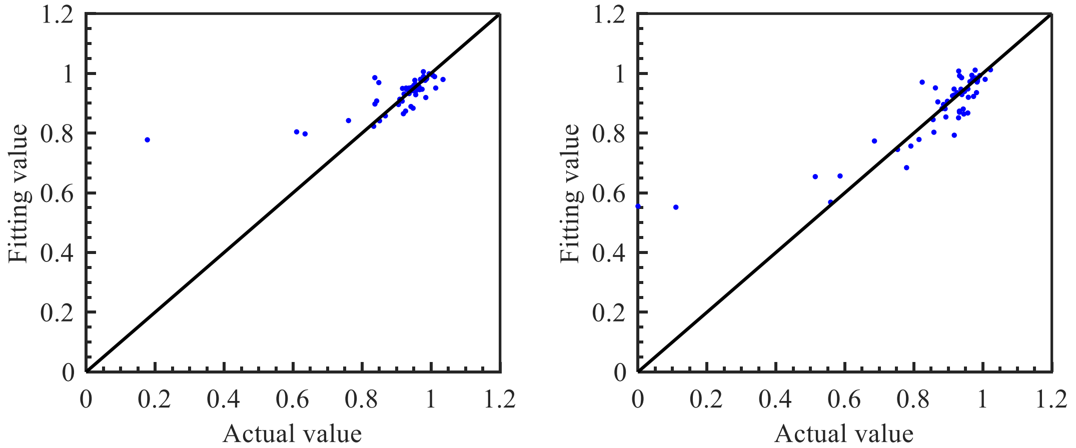

(a) Fire location 1 (b) Fire location 2

Fig. 23 Comparison between the fitting value of $k_{\Lambda,\min}$ and actual values

Table 1 Fitting parameters of $k_{\Lambda,\min}$ under common fire scenarios

Parameter	Location 1	Location 2
p_1	0.0534	0.3961
p_2	0.0205	–0.1703
p_3	–0.1550	–0.2748
p_4	0.2631	0.5988
$p_{1,1}$	–0.0459	–0.4569
$p_{1,2}$	–0.0273	0.1229
$p_{1,3}$	0.1311	0.3200
$p_{1,4}$	–0.1181	–0.3942
$p_{2,2}$	0.0303	0.1485
$p_{2,3}$	0.0521	–0.0552
$p_{2,4}$	–0.1272	–0.1364
$p_{3,3}$	–0.1550	–0.2748
$p_{3,4}$	0.1044	0.2726
$p_{4,4}$	–0.0442	–0.1622
b	0.9313	0.8820

Here we need to note that the machine learning techniques are used since the reduction factors of the ultimate bearing capacity of K6 AARSs are highly non-linear with respect to the parameters specified in Eq. (5). In this way, traditional curve-fitting techniques, although applicable, will provide complex fitting formulae. An example can be referred to in literature [20]. Besides, we aim to provide an explicit formula instead of a black box to better serve practical engineering. Therefore, we have chosen the support vector machine with a linear kernel function rather than a Gaussian kernel function or the neural networks to establish the machine learning model, though they may have a better regression performance.

However, there are still a few outliers in Fig. 23. Although this also indicates that overfitting does not exist in our trained model, we still need to emphasize that the thermal-structural coupled analysis should be conducted after determining the structural design scheme in the initial/concept design stage if the requirements proposed in Section 5.1 (for ignoring the ultimate bearing capacity analysis) are not satisfied.

5 Practical design suggestions

Besides the formula of the ultimate bearing capacity, practical design suggestions, including conditions of ignoring the ultimate bearing capacity analysis of K6 AARSs, and conditions of ignoring the radiative heat flux, are proposed in this section, aiming to reduce the computational cost of the field simulation and the thermal-structural coupled analysis.

5.1 Conditions of ignoring the ultimate bearing capacity analysis of K6 AARSs

The analysis results in Sections 3.8 and 3.9 show that the reduction in the ultimate bearing capacity under fire becomes less significant with the decrease of Q and the increase of H. Therefore, there should be a critical combination of Q and H that makes the reduction of the ultimate bearing capacity negligible. In order to explore the critical combination to simplify the calculation process, this section conducts further numerical analysis with respect to the influential parameters. Unvaried parameters include the span (40 m), number of rings (12), cross-section (H300×200×10×14), and support condition (pinned support). Influential parameters are varied according to the following scheme:

(1) Height-to-span ratio f/L: 1/3, 1/4, 1/5;
(2) Fire power Q: 2, 8, 15, 25, 35 MW;
(3) Height of supporting structure H: 20, 30, 40 m;
(4) Fire location: at the center (location 1), at the corner (location 2).

Note that the fire duration is also conservatively taken as 2400 s.

Denote k_i ($i = 1, 2$) as the minimum reduction factor of the ultimate bearing capacity of the whole fire process at the ith fire source position:

$$k_i = 1 - \frac{\Lambda_i(2400)}{\Lambda(0)} \tag{6}$$

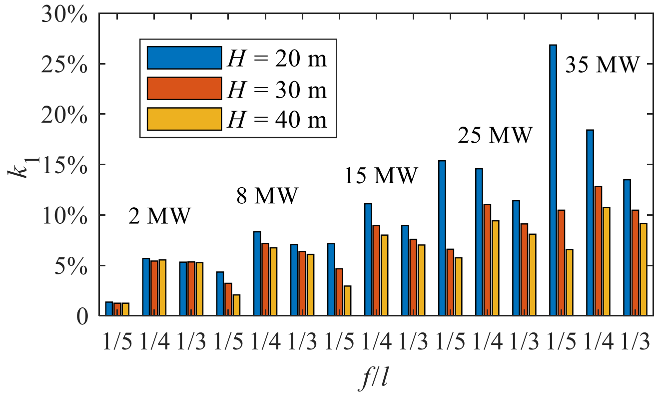

(a) Fire location 1

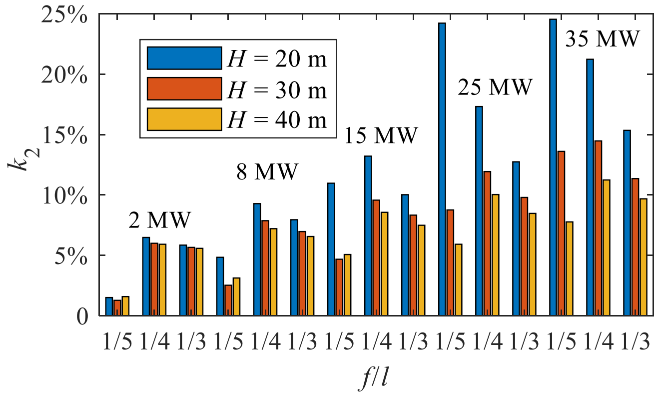

(b) Fire location 2

Fig. 24 Results of k_i

The values of k_i values from the numerical analysis are summarized in Fig. 24, and the following design suggestions can be drawn:

(1) If the designer can accept a reduction of the ultimate bearing capacity within 5 %, then when f/L equals 1/5, Q is less than or equal to 8 MW, and the minimum distance between the fire source and the structure is greater than 20 m, the ultimate bearing capacity analysis under fire can be ignored;

(2) If the designer can accept a reduction of ultimate bearing capacity within 10 %, the ultimate bearing capacity analysis under fire can be ignored when the f/L equals 1/3 or 1/5, the fire power is less than or equal to 15 MW, and the minimum distance between the fire source and the structure is greater than 20 m; when f/L is 1/4, the maximum Q should be limited to 8 MW;

(3) When Q is greater than or equal to 25 MW, the ultimate bearing capacity of the structure under fire must be conducted since the reduction in the ultimate bearing capacity is significant.

5.2 Conditions of ignoring the radiative heat flux

Zhu *et al*. [14] highlighted that the radiative heat flux plays a more important role in large-space fires compared to compartment fires, yet the contribution of the radiative heat flux to the temperature development of structural components decays with the increase of the distance between the structural component and the fire source. Therefore, this section explores the critical condition that the radiative heat flux can be ignored to provide suggestions for architectural composition and simplification of calculation. The basic model is the same as described in Section 5.1, whereas f/L and H are fixed as 1/4 and 0, respectively. Influential parameters are varied based on the following scheme:

(1) Fire power Q: 2, 8, 25 MW;
(2) Radiation heat flux: considered, ignored;
(3) Fire source-structural component distance d_f: 1, 3, 5, 7 m;
(4) Fire location: below the roof, near the support.

The fire source-structural component distance d_f refers to the distance between the centroid of the fire source and the structural components. Definitions of the fire location and d_f are shown in Fig. 25.

Since the fire source is very close to the structure, the empirical formula in reference [13] cannot be used to calculate the air temperature field. Hence, the FDS models are established using the method proposed by Zhu *et al*. [10] to calculate the air temperature field. Besides, the ultimate fire resistance time of the structure, instead of the ultimate bearing capacity, is used to evaluate the structural capacity of the structure under fire, and a uniformly-distributed surface load of 1 kN/m^2 is considered. Here we note that the fire-resistant time of the structure is defined as the moment when the stiffness matrix of the structure is singular and no further load can be applied. The fire duration is also taken as 2400 s.

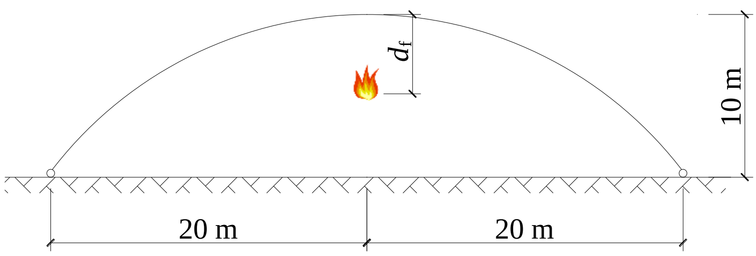

(a) Fire under the roof

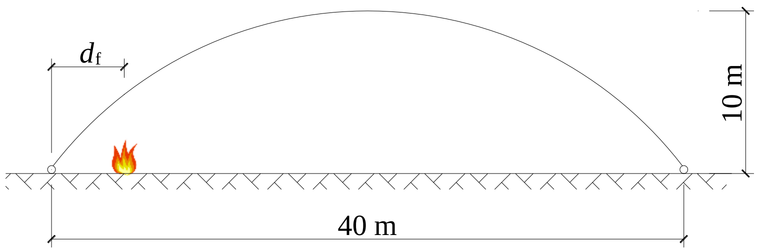

(b) Fire near the support

Fig. 25 Definitions of parametric analysis

a) Fire under the roof

The numerical analysis results when the fire is under the roof are shown in Table 2. In Table 2, t_r and t_{nr} are the ultimate fire resistance time when the radiative heat flux is considered and ignored, respectively; e_t and e_T are the relative errors of the ultimate fire resistance time and the maximum member temperature difference, defined as

$$e_t = \frac{t_{nr} - t_r}{t_r} \times 100\% \tag{7}$$

$$e_T = \max_t \left[\frac{T_{nr}(t) - T_r(t)}{T_r(t)} \right] \times 100\% \tag{8}$$

where $T_r(t)$ and $T_{nr}(t)$ are the member temperature at time t when the radiative heat flux is considered and ignored, respectively. ΔT_{max} is the maximum member temperature difference in the whole fire process, defined as

$$\Delta T_{max} = \max_t \left[T_{nr}(t) - T_r(t) \right] \tag{9}$$

Notably, e_t is negative only when Q is 8 MW and d_f is 5 m, indicating the ultimate fire resistance time is increased by considering the radiative heat flux. Figs. 26 and 27 plot the member temperature contours at the ultimate state of the structure when Q is 8 MW, and d_f is 1 m and 5 m, respectively. It can be seen from Fig. 26 that the peak temperature of the structure increases dramatically. In contrast, the peak temperature only increases slightly in Fig. 27, and the member temperature field is also changed. As the thermal expansion becomes more uniform for the state of Fig. 27(a), t_r is prolonged to be larger than t_{nr}. Therefore, in order to ensure the accuracy of structural fire analysis results, the influence of radiative heat flux should be considered when calculating the temperature development of structural components.

Table 2 Parameter analysis results when the fire is under the roof.

Q / MW	d_f / m	t_r / s	t_{nr} / s	e_t / %	ΔT_{max} / °C	e_T / %
2	1	161	187	16.15	–55	–51.43
2	3	408	408	0.00	–17	–20.53
2	5	2400	2400	0.00	–7	–10.63
2	7	2400	2400	0.00	–4	–6.28
8	1	132	216	63.64	–207	–80.63
8	3	262	350	33.59	–53	–50.70
8	5	410	396	–3.41	–23	–32.19
8	7	432	449	3.94	–13	–21.13
25	1	38	187	392.11	–498	–92.54
25	3	178	305	71.35	–162	–76.04
25	5	394	415	5.33	–71	–59.59
25	7	418	430	2.87	–50	–45.49

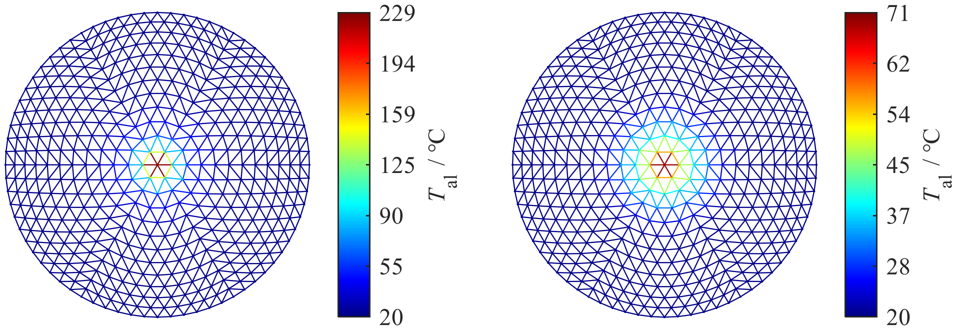

(a) Radiative heat flux considered (b) Radiative heat flux ignored

Fig. 26 Member temperature contour of the structure at 132 s (Q = 8 MW and d_f = 1 m)

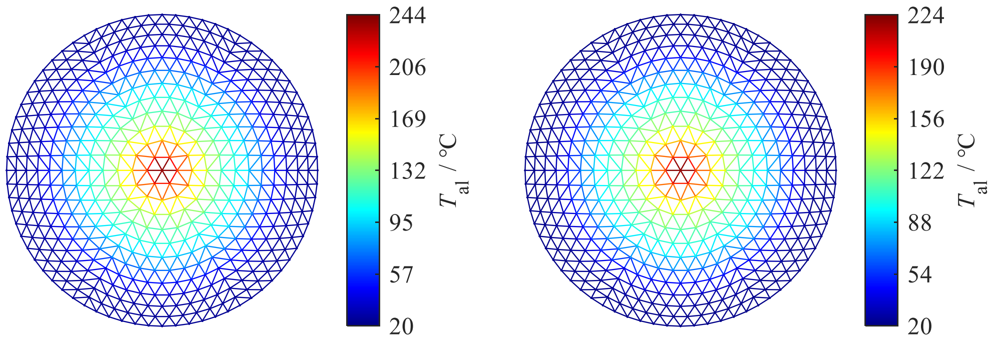

(a) Radiative heat flux considered (b) Radiative heat flux ignored

Fig. 27 Member temperature contour of the structure at 396 s (Q = 8 MW and d_f = 5 m)

Nonetheless, the relationship of $t_r \leq t_{nr}$ holds for other situations. Based on the data in Table 2, it can be concluded that if the designer can accept a maximum of 10 % of e_t, the radiative heat flux (when the fire is under the roof) can be ignored when d_f is greater than the critical value $d_{f,min,r}$:

$$d_{\mathrm{f,min,r}} = \begin{cases} 3 & Q \le 2 \\ \dfrac{1}{3}\left(Q+7\right) & 2 < Q < 8 \\ 5 & 8 \le Q \le 25 \end{cases} \tag{10}$$

b) Fire near the support

The numerical analysis results when the fire is under the roof are shown in Table 3, where the relationship of $t_{\mathrm{r}} \le t_{\mathrm{nr}}$ holds for all situations. By comparing Tables 2 and 3, it can be concluded that when the fire is located near the support, the effect of increasing d_{f} on improving the ultimate fire resistance time of the structure is more significant than that when the fire is below the roof.

Similarly, according to the results of Table 3, it can be concluded that if the designer can accept a maximum of 10 % of e_{t}, the radiative heat flux (when the fire is near the support) can be ignored when d_{f} is greater than the critical value $d_{\mathrm{f,min,s}}$:

Table 3 Parameter analysis results when the fire is near the support

Q / MW	d_{f} / m	t_{r} / s	t_{nr} / s	e_{t} / %	ΔT_{max} / °C	e_{T} / %
2	1	382	2400	528.27	–252	–81.71
2	3	2400	2400	0.00	–38	–52.82
2	5	2400	2400	0.00	–16	–30.97
2	7	2400	2400	0.00	–9	–19.68
8	1	72	2400	3233.33	–504	–94.18
8	3	2400	2400	0.00	–148	–81.54
8	5	2400	2400	0.00	–64	–64.08
8	7	2400	2400	0.00	–35	–49.41
25	1	20	2400	11900.00	–539	–96.36
25	3	252	2400	852.38	–413	–92.87
25	5	1630	2400	47.24	–194	–84.59
25	7	2400	2400	0.00	–109	–75.15

$$d_{\mathrm{f,min,s}} = \begin{cases} 3 & Q \le 8 \\ \dfrac{1}{17}\left(4Q+19\right) & 8 < Q \le 25 \end{cases} \tag{11}$$

When d_{f} is small, the adverse effect of the radiative heat flux will significantly reduce the ultimate fire resistance time of the structure. Therefore, Eqs. (10) and (11) are suggested to be referred to in order to limit the minimum values of d_{f} when conducting architectural composition to determine the fire scenarios.

6 Conclusions

Based on the existing research findings on the high-temperature mechanical performance of aluminum alloy materials and structural components, this paper conducts numerical analyses of AARSs under fire conditions considering joint semi-rigidity. The main contributions or conclusions are as follows:

(1) The numerical model of AARSs under fire conditions considering joint semi-rigidity is established and verified against the room-temperature test and the fire tests. It is notable that the proposed model can also be applied to the thermal-structural coupled analysis of other structures with semi-rigid joints;

(2) The reduction factor of the ultimate bearing capacity of K6 AARSs under common fire conditions is related to the span, the height-to-span-ratio f/L, the height of the supporting structure, and the fire power Q, while it is independent of the number of element divisions, the number of rings, the span-to-thickness ratio, and the support condition. The main mechanism of this phenomenon is that the failure of AARSs is highly associated with extra compressive force at the outmost ring induced by the ferrule effect, and the influential parameters will affect the relative stiffness of the outmost ring under fire conditions;

(3) The reduction in the ultimate bearing capacity of K6 AARSs is rapid at the stable combustion stage of the fire duration and is slow at the initial and decay stages;

(4) Practical design formulae are derived by machine learning via 324 thermal-structural coupled analysis results to serve the initial/concept design of K6 AARSs.

(5) Conditions of ignoring the ultimate bearing capacity of K6 AARSs are proposed. Specifically, if the designer can accept a reduction in the ultimate bearing capacity within 5 %, the conditions are: f/L = 1/5, $Q \leq 8$ MW, and the minimum distance between the fire source and the structure is greater than 20 m. If the designer can accept a reduction in the ultimate bearing capacity within 10 %, the conditions are f/L = 1/3 or 1/5, $Q \leq 15$ MW, and the minimum distance between the fire source and the structure is greater than 20 m; when f/L = 1/4, the maximum Q should be limited to 8 MW;

(6) Conditions of ignoring the radiative heat flux are proposed by limiting the minimum value of the distance between the centroid of the fire source and the structural component d_f. It is notable that the limit values of d_f are suggested to be referred to in order to limit the minimum values of d_f when conducting architectural composition to determine the fire scenarios. This conclusion can

be referred to when designing AARSs with any structural forms.

Statements and Declarations

The authors declare that they have no known competing financial interests or personal relationships that could have appeared to influence the work reported in this paper.

Data Availability Statement

Some or all data, models, or codes that support the findings of this study are available from the corresponding author upon reasonable request.

Acknowledgments

The authors gratefully acknowledge the financial support provided by the National Natural Science Foundation of China under grant No. 51478335.

References

[1] Meacham BJ, Custer RLP. Performance-based fire safety engineering: An introduction of basic concepts. J Fire Prot Eng. 1995; 7(2): 35-53. https://doi.org/10.1177/104239159500700201

[2] Roy K, Lim JBP, Lau HH, Yong PM, Cliftona GC, Johnston Ross PD, Wrzesien A, Mei CC. Collapse behaviour of a fire engineering designed single-storey cold-formed steel building in severe fires. Thin-Walled Struct. 2019; 142: 340-357. https://doi.org/10.1016/j.tws.2019.04.046

[3] Du E. Experimental and theoretical research on the structural behavior of large space steel structures subjected to natural fires. Nanjing: Southeast University; 2016. (in Chinese)

[4] Lou G, Wang C, Jiang J, Jiang Y, Wang L, Li G. Experimental and numerical study on thermal-structural behavior of steel portal frames in real fires. Fire Safety J. 2018; 98: 48-62. https://doi.org/10.1016/j.firesaf.2018.04.006

[5] Lou G, Wang C, Jiang J, Jiang Y, Wang L, Li G. Fire tests on full-scale steel portal frames against progressive collapse. Journal of Constr Steel Res. 2018; 145: 137-152. https://doi.org/10.1016/j.jcsr.2018.02.024

[6] Alos-Moya J, Paya-Zaforteza I, Hospitaler A, Rinaudo P. Valencia bridge fire tests: Experimental study of a composite bridge under fire. Journal of Constr Steel Res. 2017; 138: 538-554. https://doi.org/10.1016/j.jcsr.2017.08.008

[7] Chen C, Zhang D, Zhang W, Shen B. Experimental behaviors of steel staggered-truss system exposed to fire under lateral force. Int J Steel Struct, 2012; 12(1): 59-70.
https://doi.org/10.1007/s13296-012-1006-1

[8] Liu M, Zhao J, Jin M. An experimental study of the mechanical behavior of steel planar tubular trusses in a fire. Journal of Constr Steel Res. 2010; 66(4): 504-511.
https://doi.org/10.1016/j.jcsr.2009.11.005

[9] Guo X, Zhu S, Jiang S, Zhang C, Chen C. Fire tests on single-layer aluminum alloy reticulated shells with gusset joints. Structures. 2020; 28: 1137-1152.
https://doi.org/10.1016/j.istruc.2020.09.054

[10] Zhu S, Guo X, Jiang S, Zong S, Chen C. Experimental study on the fire-induced collapse of single-layer aluminum alloy reticulated shells with gusset joints. J Struct Eng-ASCE. 2020; 146(12): 04020268.
https://doi.org/10.1061/(ASCE)ST.1943-541X.0002819

[11] Yin L, Ni Z, Fan F, Qiu P, Kan Q, Ouyang Y. Temperature field characteristics of cylindrical aluminum alloy reticulated roof system under localized fire. Fire Safety J. 2021; 121: 103267.
https://doi.org/10.1016/j.firesaf.2020.103267

[12] Yin L, Ni Z, Fan F, Ye J. Current status analysis of fire protection design system of long-span spatial structures. Fire Sci Technol. 2018; 37: 1178-1180. (in Chinese)

[13] Du Y, Li G. A new temperature-time curve for fire-resistance analysis of structures. Fire Safety J. 2012, 54: 113-120.
https://doi.org/10.1016/j.firesaf.2012.07.004

[14] Zhu S, Guo X, Tang W, Gao S, Chen C. Temperature development of aluminum alloy members considering fire radiation. J Build Eng. 2021; 42: 102836.
https://doi.org/10.1016/j.jobe.2021.102836

[15] Guo X, Xiong Z, Luo Y, Qiu L, Liu J. Experimental investigation on the semi-rigid behaviour of aluminium alloy gusset joints. Thin-Walled Struct. 2015; 87: 30-40.
https://doi.org/10.1016/j.tws.2014.11.001

[16] Xiong Z, Guo X, Luo Y, Xu H. Numerical analysis of aluminium alloy gusset joints subjected to bending moment and axial force. Eng Struct, 2017; 152: 1-13.
https://doi.org/10.1016/j.engstruct.2017.09.005

[17] Zhang Y, Wang Y, Li B, Wang Z, Liu X, Zhang J, Ouyang Y. Structural behaviour of the aluminium alloy Temcor joints and Box-I section hybrid gusset joints under combined bending and shear. Eng Struct. 2021; 249: 113380.
https://doi.org/10.1016/j.engstruct.2021.113380

[18] Liu H, Du P, Chen Z, Xu F. Mechanical properties of T-plate stiffened gusset joints

for aluminum alloy single layer two-way grid shells. J Build Eng. 2021; 44: 103249. https://doi.org/10.1016/j.jobe.2021.103249

[19] Liu H, Ding Y, Chen Z. Static stability behavior of aluminum alloy single-layer spherical latticed shell structure with Temcor joints. Thin-Walled Struct. 2017; 120: 355-365. https://doi.org/10.1016/j.tws.2017.09.019

[20] Xiong Z, Guo X, Luo Y, Zhu S. Elasto-plastic stability of single-layer reticulated shells with aluminium alloy gusset joints. Thin-Walled Struct. 2017; 115: 163-175. https://doi.org/10.1016/j.tws.2017.02.008

[21] Xiong Z, Zhu S, Zou X, Guo S, Qiu Y, Li L. Elasto-plastic buckling behaviour of aluminium alloy single-layer cylindrical reticulated shells with gusset joints. Eng Struct. 2021; 242: 112562. https://doi.org/10.1016/j.engstruct.2021.112562

[22] Guo X, Zhu S, Liu X, Wang K. Study on out-of-plane flexural behavior of aluminum alloy gusset joints at elevated temperatures. Thin-Walled Struct. 2018; 123: 452-466. ttps://doi.org/10.1016/j.tws.2017.11.045

[23] Xiong Z, Guo X, Luo Y, Zhu S, Liu J. Experimental and numerical studies on single-layer reticulated shells with aluminium alloy gusset joints. Thin-Walled Struct. 2017; 118: 124-136. https://doi.org/10.1016/j.tws.2017.05.007

[24] Design of aluminum alloy structures - part 1-2: structural fire design: EN1999-1-2 Eurocode 9. Brussels: European Committee for Standardization; 2007.

[25] Ansys Inc. ANSYS® Multiphysics 19.0. Canonsburg, Pennsylvania, USA, 2018.

[26] Guo X, Xiong Z, Luo Y, Qiu L, Huang W. Application of the component method to aluminum alloy gusset joints. Adv Struct Eng, 2015; 18(11): 1931-1946. https://doi.org/10.1260/1369-4332.18.11.1931

[27] Zhu S, Guo X, Liu X, Gao S. The in-plane effective length of members in aluminum alloy reticulated shell with gusset joints. Thin-Walled Struct. 2018; 123: 483-491. https://doi.org/10.1016/j.tws.2017.10.033

[28] Ministry of Construction of the People's Republic of China. Code for design of aluminium structures GB 50429-2007. Beijing: China Planning Press; 2012. (in Chinese)

[29] Hurley M J. NFPA SFPE Handbook of Fire Protection Engineering (fifth edition). New York: Springer; 2015.

[30] Fan F, Yan J, Cao Z. Stability of reticulated shells considering member buckling.

Journal of Constr Steel Res. 2012; 77: 32-42. https://doi.org/10.1016/j.jcsr.2012.04.011

[31] Zhu S, Ohsaki M, Guo X. Prediction of non-linear buckling load of imperfect reticulated shell using modified consistent imperfection and machine learning. Eng Struct. 2021; 226: 111374. https://doi.org/10.1016/j.engstruct.2020.111374

[32] Zhu S, Ohsaki M, Guo X, Zeng Q. Shape optimization for non-linear buckling load of aluminum alloy reticulated shells with gusset joints. Thin-Walled Struct. 2020; 154:106830. https://doi.org/10.1016/j.tws.2020.106830

[33] Mathworks. Statistics and Machine learning Toolbox User's Guide R2020a, 2020.